














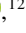






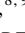




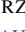





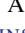

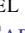





TOI-2005b: An Eccentric Warm Jupiter in Spin-Orbit Alignment

ALLYSON BIERYLA ^{1,2} JIAYIN DONG ^{3,4,*} GEORGE ZHOU ² JASON D. EASTMAN ¹ L. C. MAYORGA ⁵
DAVID W. LATHAM ¹ BRAD CARTER ² CHELSEA X. HUANG ² SAMUEL N. QUINN ¹ KAREN A. COLLINS ¹
LYU ABE ⁶ YURI BELETSKY ⁷ RAFAEL BRAHM ^{8,9,10} KNICOLE D. COLÓN ¹¹ ZAHRA ESSACK ¹² TRISTAN GUILLOT ⁶
THOMAS HENNING ¹³ MELISSA J. HOBSON ^{13,9} KEITH HORNE ¹⁴ JON M. JENKINS ¹⁵ MATÍAS I. JONES ¹⁶
ANDRÉS JORDÁN ^{8,9,10} DAVID OSIP ⁷ GEORGE R. RICKER ¹⁷ JOSEPH E. RODRIGUEZ ¹⁸ JACK SCHULTE ¹⁸
RICHARD P. SCHWARZ ¹ SARA SEAGER ^{17,19,20} AVI SHPORER ¹⁷ OLGA SUAREZ ²¹ THIAM-GUAN TAN ²²
ERIC B. TING ¹⁵ AMAURY TRIAUD ²³ ANDREW VANDERBURG ¹⁷ JESUS NOEL VILLASEÑOR ²⁴ NOAH VOWELL ^{18,1}
CRISTILYN N. WATKINS ¹ JOSHUA N. WINN ²⁵ AND CARL ZIEGLER ²⁶

¹Center for Astrophysics | Harvard & Smithsonian, 60 Garden Street, Cambridge, MA 02138, USA

²University of Southern Queensland, Centre for Astrophysics, West Street, Toowoomba, QLD 4350 Australia

³Center for Computational Astrophysics, Flatiron Institute, 162 Fifth Avenue, New York, NY 10010, USA

⁴Department of Astronomy, University of Illinois at Urbana-Champaign, Urbana, IL 61801, USA

⁵The Johns Hopkins University Applied Physics Laboratory, 11100 Johns Hopkins Rd, Laurel, MD, 20723, USA

⁶Observatoire de la Côte d'Azur, UniCA, Laboratoire Lagrange, CNRS UMR 7293, CS 34229, 06304 Nice cedex 4, France

⁷Las Campanas Observatory, Carnegie Institution for Science, Colina El Pino, Casilla 601 La Serena, Chile

⁸Facultad de Ingeniería y Ciencias, Universidad Adolfo Ibáñez, Av. Diagonal las Torres 2640, Peñalolén, Santiago, Chile

⁹Millennium Institute for Astrophysics, Chile

¹⁰Data Observatory Foundation, Chile

¹¹NASA Goddard Space Flight Center, Exoplanets and Stellar Astrophysics Laboratory (Code 667), Greenbelt, MD 20771, USA

¹²Department of Physics and Astronomy, The University of New Mexico, 210 Yale Blvd NE, Albuquerque, NM 87106, USA

¹³Max-Planck-Institut für Astronomie, Königstuhl 17, 69117 Heidelberg, Germany

¹⁴SUPA Physics and Astronomy, University of St. Andrews, Fife, KY16 9SS Scotland, UK

¹⁵NASA Ames Research Center, Moffett Field, CA 94035, USA

¹⁶European Southern Observatory, Alonso de Córdova 3107, Vitacura, Casilla, 19001, Santiago, Chile

¹⁷Department of Physics and Kavli Institute for Astrophysics and Space Research, Massachusetts Institute of Technology, Cambridge, MA 02139, USA

¹⁸Center for Data Intensive and Time Domain Astronomy, Department of Physics and Astronomy, Michigan State University, East Lansing, MI 48824, USA

¹⁹Department of Earth, Atmospheric and Planetary Sciences, Massachusetts Institute of Technology, Cambridge, MA 02139, USA

²⁰Department of Aeronautics and Astronautics, MIT, 77 Massachusetts Avenue, Cambridge, MA 02139, USA

²¹Observatoire de la Côte d'Azur, UniCA, CNRS, CS 34229, 06304 Nice cedex 4, France

²²Perth Exoplanet Survey Telescope, Perth, Western Australia, Australia

²³School of Physics & Astronomy, University of Birmingham, Edgbaston, Birmingham, B15 2TT, UK

²⁴Department of Physics and Kavli Institute for Astrophysics and Space Research, Massachusetts Institute of Technology, Cambridge, MA 02139, USA

²⁵Department of Astrophysical Sciences, Princeton University, 4 Ivy Lane, Princeton, NJ 08544, USA

²⁶Department of Physics, Engineering and Astronomy, Stephen F. Austin State University, 1936 North St, Nacogdoches, TX 75962, USA

ABSTRACT

We report the discovery and characterization of TOI-2005 b, a warm Jupiter on an eccentric ($e \sim 0.59$), 17.3-day orbit around a $V_{\text{mag}} = 9.867$ rapidly rotating F-star. The object was detected as a candidate by TESS and the planetary nature of TOI-2005 b was then confirmed via a series of ground-based photometric, spectroscopic, and diffraction-limited imaging observations. The planet was found to reside in a low sky-projected stellar obliquity orbit ($\lambda = 4.8_{-2.5}^{+2.3}$ degrees) via a transit spectroscopic observation using the Magellan MIKE spectrograph. TOI-2005 b is one of a few planets known to have a low-obliquity, high-eccentricity orbit, which may be the result of high-eccentricity coplanar migration. The planet has a periastron equilibrium temperature of ~ 2100 K, similar to some highly irradiated hot Jupiters where atomic metal species have been detected in transmission

spectroscopy, and varies by almost 1000 K during its orbit. Future observations of the atmosphere of TOI-2005b can inform us about its radiative timescales thanks to the rapid heating and cooling of the planet.

Keywords: Extrasolar gaseous giant planets (509) — Radial velocity (1332) — Transit photometry (1709)

1. INTRODUCTION

Unlike the case for hot Jupiters, the orbital eccentricities and inclinations of warm Jupiters, planets with $a/R_\star > 10$ and $R_p > 8 R_e$, may preserve clues to the dynamical histories of close-in giant planets. This is because warm Jupiters experience relatively weak tidal interactions between the planet and its parent star, which would otherwise reduce the eccentricity and inclination. Thus, the orbital parameters of warm Jupiter systems are one avenue to decipher the mechanisms that drive the formation and orbital evolution of Jupiter systems.

Only six transiting warm Jupiters with eccentricities larger than 0.5 have had their projected spin-orbit angles measured thus far (Figure 8). Within this small sample, only two (TOI-1859b; Dong et al. 2023 and TOI-3362b; Dong et al. 2021; Espinoza-Retamal et al. 2023a) orbit stars with $T_{\text{eff}} > 6250$ K. Early-type stars have little to no convective envelope and the obliquity of the system is therefore unlikely to be altered by tidal interactions (Winn et al. 2010). Thus, when restricting attention to such hot stars, it may be easier to interpret the comparison between the spin-orbit angles of warm Jupiters and those of hot Jupiters, making obliquity measurements a particularly useful tracer for formation and evolution mechanisms.

High-eccentricity tidal migration is thought to be the primary source of eccentric warm Jupiters which are thought to be planets that avoided tidal circularization via close periastron passages to form hot Jupiters (see review by Dawson & Johnson 2018). Possible dynamical drivers include planet-planet scattering (e.g. Rasio & Ford 1996; Chatterjee et al. 2008; Nagasawa et al. 2008), secular interactions, such as von Zeipel-Lidov-Kozai oscillations (von Zeipel 1910; Lidov 1962; Kozai 1962) and secular chaos (Wu et al. 2023). These mechanisms all predict a wide distribution of orbital obliquities for the resulting planet population.

In this paper, we report the planetary confirmation of TOI-2005 b, a warm Jupiter on a 17.3-day eccentric orbit that is well aligned with the equatorial plane of a rapidly rotating F-star. In Section 2, we describe the photometric data from *TESS* and multiple ground-based observatories, high-resolution speckle imaging, and CHIRON, FEROS, MINERVA-Australis, and Magellan-MIKE spectroscopic observations used to measure the stellar obliquity and

to obtain an upper limit on the planetary mass. Section 3 describes the global modeling of the system to derive system parameters. We conclude with a discussion of the system and future atmospheric observational prospects in Section 4.

2. OBSERVATIONS

2.1. Photometric Observations

2.1.1. *TESS* Photometry

Launched in April of 2018, the Transiting Exoplanet Survey Satellite (*TESS*; Ricker et al. 2015) is performing an all-sky survey in search of transiting exoplanets around nearby bright host stars. Each sector of observations is approximately 27 days in length and spans 24×96 degrees of the sky at a time. TOI-2005 (TIC 147660886) was observed by *TESS* in Sectors 9 and 10 of Year 1 of the primary mission with 1800-second cadence. It was then re-observed in the extended mission in Sector 36 during Year 3 at 120-second and 600-second cadences and in Sector 63 during year 5 at a 20-second, 120-second, and 200-second cadences. The data were processed by the NASA Science Processing Operations Center pipeline (SPOC; Jenkins et al. 2016) and the light curves were downloaded from the Mikulski Archive for Space Telescopes (MAST)¹ using the *Lightkurve* package (Lightkurve Collaboration et al. 2018). The Presearch Data Conditioning Simple Aperture Photometry (PDCSAP; Stumpe et al. 2012, 2014; Smith et al. 2012)) light curves were employed in our analysis and are plotted in Figure 1. All *TESS* mission data used in this paper can be found in MAST: <https://doi:10.17909/fwdt-2x66>.

The SPOC (Jenkins et al. 2016) and QLP (Huang et al. 2020; Kunimoto et al. 2022) pipelines identified a 17.3d candidate exoplanet orbiting TOI-2005. The SPOC performed a transit search with an adaptive, noise-compensating matched filter (Jenkins 2002; Jenkins et al. 2010, 2020), producing a Threshold Crossing Event (TCE) for which an initial limb-darkened transit model was fitted (Li et al. 2019) and a suite of diagnostic tests were conducted to help assess the planetary nature of the signal (Twicken et al. 2018). The transit signature was first detected in a search of Full Frame Image (FFI) data by the QLP pipeline at MIT. The QLP performed its transit search with the Box Least Squares Algorithm (Kovács et al. 2002). The *TESS* Science Office (TSO) reviewed the vetting information and issued an alert on 17

* Flatiron Research Fellow

¹ <https://mast.stsci.edu/portal/Mashup/Clients/Mast/Portal.html>

June 2020 (Guerrero et al. 2021). The difference image centroid offsets localized the transit source for TOI 2005.01 within 2.4 ± 2.5 arcsec. The light curves were made available as part of SPOC processing of the TESS-SPOC science products (Caldwell et al. 2020).

2.1.2. Ground-based Photometry

Follow-up ground-based photometric observations were performed by several observatories to aid in the confirmation of TOI-2005 b as part of the TESS Follow-up Observing Program² Sub Group 1 (TFOP; Collins 2019). On-target high resolution observations confirmed that the signal comes from the target and that there were no nearby eclipsing binaries that could potentially be contaminating the *TESS* photometry. The *TESS* Transit Finder, a customized version of the *Tapir* software package (Jensen 2013), was used to schedule ground-based transit observations. *AstroImageJ* (AIJ, Collins et al. 2017) was used for the data reduction and aperture photometry unless otherwise noted. A short description of each facility is below and a summary of all the photometric observations can be found in Table 1. The phase folded lightcurves are shown in Figure 2. All light curve data are available on the EXOFOP-TESS website³ and are included in the global modeling described in Section 3. Two datasets from the Perth Exoplanet Survey Satellite (PEST) Observatory were excluded from the global fits due to poor observing conditions.

We observed two full transit windows of TOI-2005.01 in Pan-STARRS *z*-short band on UT 2021 March 03 and 2021 April 23 from the Las Cumbres Observatory Global Telescope (LCOGT; Brown et al. 2013) 1 m network node at Cerro Tololo Inter-American Observatory in Chile (CTIO). Another full transit window was observed in Pan-STARRS *z*-short band on UT 2022 May 09 from the LCOGT 1 m network node at South Africa Astronomical Observatory near Sutherland, South Africa (SAAO). The 1 m telescopes are equipped with 4096×4096 SINISTRO cameras with an image scale of $0''.389$ per pixel, resulting in a $26' \times 26'$ field-of-view. The images were calibrated by the standard LCOGT BANZAI pipeline (McCully et al. 2018), and differential photometric data were extracted using *AstroImageJ*. We used circular photometric aperture radii of $5''.8$, $6''.6$, and $5''.1$, respectively, that excluded all of the flux from the nearest known neighbor in the Gaia DR3 catalog (Gaia DR3 5388416255317688064) that is $10''.7$ east of TOI-2005. An \sim on-time ~ 3 ppt event was detected in all three observations.

On UT 2021 May 11, a full transit of TOI-2005.01 was observed with ASTEP (Antarctic Search for Transiting Exoplanets) (Guillot et al. 2015), with a broad R filter between

about 550 and 800 nm (Abe et al. 2013) and 25 second exposures. Data processing was done as described in Mékarnia et al. (2016). The event was seen on time with a measured duration of 4:12 hours and a measured depth of ~ 2.6 ppt for an uncontaminated $11.2''$ aperture radius, consistent with expectations from TESS. ASTEP also re-observed a full transit on UT 2022 April 22, this time using a new camera operating between 700 and 1000 nm (Schmider et al. 2022) and 8 second exposures. The transit was again detected as predicted, with a similar depth and duration.

On UT 2023 May 07, we observed an ingress of TOI-2005.01 with the Goodman High Throughput Spectrograph (in imaging mode) on the SOuthern Astrophysical Research (SOAR) telescope (Clemens et al. 2004) at Cerro Tololo Interamerican Observatory in Chile. Because TOI-2005 is brighter in red wavelengths, we chose to utilize the Goodman Red camera for these observations, which is a 4096×4112 pixel charge-coupled device (CCD) detector with a spatial resolution of $0.15''/\text{pixel}$. Our observations were collected in the *z'* filter with an exposure time of 11-seconds. The images were then calibrated and reduced using *AstroImageJ*. No nearby known sources were included in the photometric aperture.

2.1.3. High-resolution Imaging

High-angular resolution imaging is needed to search for nearby sources that can contaminate the TESS photometry, resulting in an underestimated planetary radius, or be the source of astrophysical false positives, such as background eclipsing binaries. We searched for stellar companions to TOI-2005 with speckle imaging on the 4.1-m Southern Astrophysical Research (SOAR) telescope (Tokovinin 2018) on 31 October 2020 UT, observing in Cousins I-band, a similar visible bandpass as TESS. This observation was sensitive enough to detect a 5.6-magnitude fainter star at an angular distance of 1 arcsec from the target. More details of the observations within the SOAR TESS survey are available in Ziegler et al. (2020). The 5σ detection sensitivity and speckle auto-correlation functions from the observations are shown in Figure 3. No nearby stars were detected within $3''$ of TOI-2005 in the SOAR observations.

2.2. Spectroscopic Observations

A total of 46 spectra were obtained from three separate observatories between UT 2020 March 20 and 2023 April 23. Details about the spectroscopic observations from each facility are described in more detail below. All radial velocities were derived via an analysis of the spectroscopic line profiles from least-squares deconvolutions. The observed spectra were deconvolved against a matching non-rotating synthetic template from the ATLAS9 model atmospheres (Castelli & Kurucz 2004). The resulting line profiles were modeled with a set of kernels representing contributions from

² <https://tess.mit.edu/followup>

³ <https://exofop.ipac.caltech.edu/tess/target.php?id=147660886>

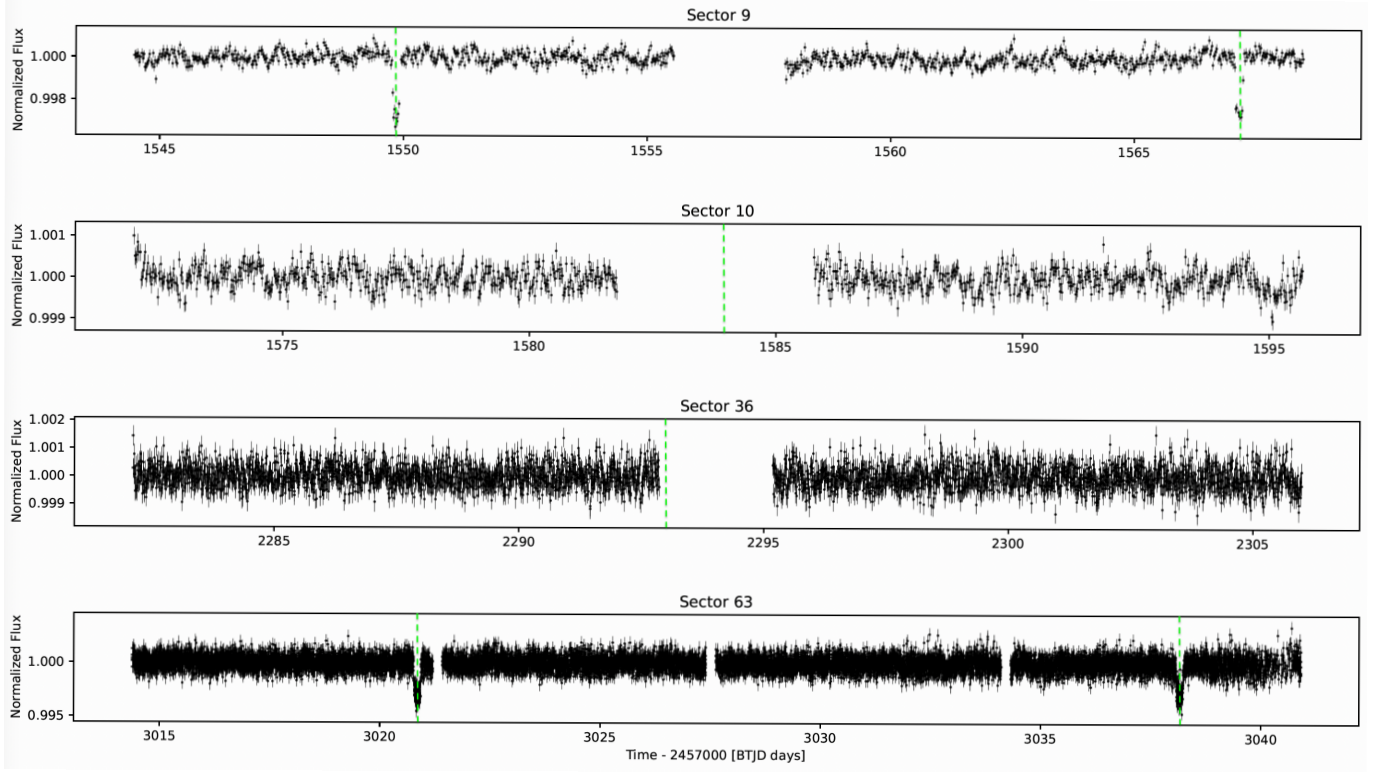


Figure 1. Per-sector Normalized TESS PDCSAP light curves for TOI-2005. The target star was observed over four TESS sectors. The observing cadence was 1800 seconds in Sectors 9 and 10, 600 seconds in Sector 36, and 200 seconds in Sector 63. Unfortunately, during Sectors 10 and 36 the transit occurred in the gap in the lightcurve during data download. Predicted transits are marked with vertical dashed green lines.

Table 1. Ground-based Photometry

Observatory	Telescope size meters	Camera	Filter	Pixel Scale arseconds	UT Date yyyy-mm-dd	Detrend Parameters
LCO-CTIO	1.0	SINESTRO	z'	0.39	2021-03-03	focus position
LCO-CTIO	1.0	SINESTRO	z'	0.39	2021-04-23	none
ASTEP	0.4	FLI Proline 16800E	R_c	0.93	2021-05-11	airmass
LCO-SAAO	1.0	SINISTRO	z'	0.39	2022-05-09	sky/pixel, $Y(\text{fits})_{T1}$
SOAR	4.1	Goodman HTS	z'	0.15	2023-05-07	airmass, width_{T1}

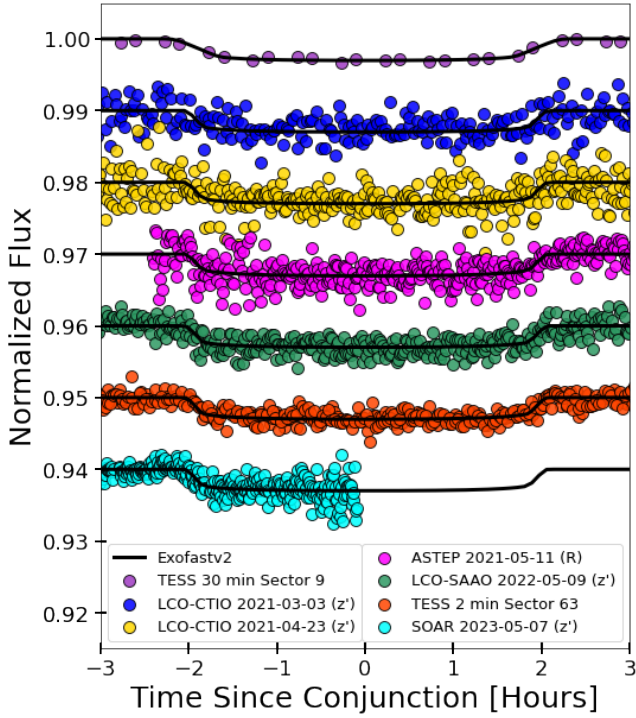


Figure 2. Ground-based and TESS lightcurves normalized and offset relatively in flux and phased in time to the best-fit ephemeris. The best-fit model is shown in black.

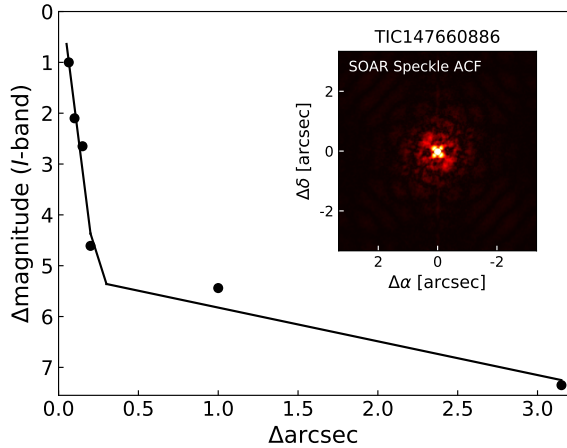


Figure 3. 5σ detection sensitivity and speckle auto-correlation functions of TOI-2005 from the 4.1-m SOAR. We find no companions to TOI-2005 within $3''$ in these high resolution imaging observations.

rotation, macroturbulence, instrumental broadening, and radial velocity shift as per Gray (2005). The velocity shifts applied to the kernels are the radial velocities of the star. These radial velocities are then combined order to order, as is standard for cross-correlation-function derived velocities, to determine the per-epoch velocity and uncertainty of the observation. The radial velocities are listed in Table 2 and the

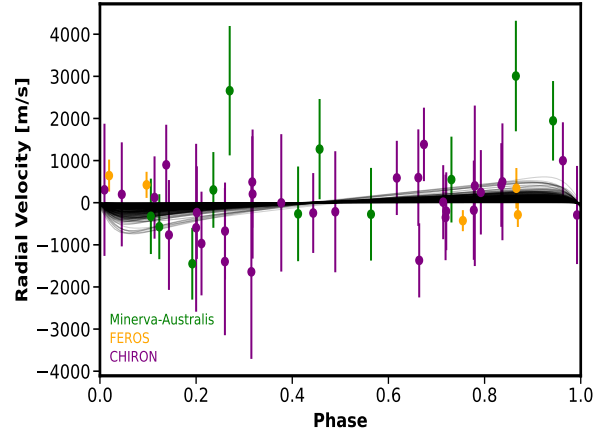


Figure 4. Radial velocity observations phase folded to the ephemeris. Section 2.2 details the radial velocities observations. Over-plotted are 500 realizations of the converged models from the global modeling, illustrating the set of velocity orbits allowed by the transit and radial velocity observations, illustrating the constraint placed on eccentricity by the joint model. The 3σ radial velocity semi-amplitude of 1320 m s^{-1} provided a 3σ upper mass limit on the companion of $6.4M_{\text{Jup}}$.

phase folded velocities are shown in Figure 4, along with 500 realizations of the converged models from Section 3. We also applied the Least Squares Deconvolution technique to the CHIRON spectra to determine the stellar rotational velocity. The analysis revealed an average $v \sin I_*$ of $111 \pm 1 \text{ km s}^{-1}$.

2.2.1. CHIRON

CHIRON is a fiber-fed echelle spectrograph on the 1.5m SMARTS telescope at Cerro Tololo Inter-American Observatory, Chile (Tokovinin et al. 2013). CHIRON observes over the wavelength range $4100 - 8200 \text{ \AA}$ and has a spectral resolving power of $R \sim 80,000$. Spectra were extracted as per the official CHIRON pipeline (Paredes et al. 2021). Thirty observations were obtained between March 2020 and April 2023.

2.2.2. FEROS

The Fiber-fed Extended Range Optical Spectrograph (FEROS Kaufer et al. 1999) is a high resolution, temperature stabilized echelle spectrograph installed at the MPG-2.2m telescope, in the ESO La Silla Observatory, in Chile. FEROS has a resolving power of 48,000 and uses a second fiber to trace instrumental wavelength shifts. We obtained 5 FEROS spectra between between December 2020 and January 2024 in the context of the Warm glaNts with tEes collaboration (WINE Brahm et al. 2019; Jordán et al. 2020a; Hobson et al. 2023; Jones et al. 2024). The adopted exposure time was 300-second and the typical signal-to-noise ratio was of 120. All reduction and processing steps were performed using the *ceres* pipeline (Brahm et al. 2017).

Table 2. Radial Velocities

Time [BJD _{TDB}]	Velocity [km s ⁻¹]	Uncertainty [km s ⁻¹]	Spectrograph
2458918.71188	7.89	2.07	CHIRON
2458921.73230	9.32	1.44	CHIRON
2458925.61713	9.54	0.88	CHIRON
2459187.83937	-6.35	0.48	FEROS
2459191.83386	-6.27	0.31	FEROS
2459207.79145	-6.05	0.38	FEROS
2459209.84761	8.37	0.95	CHIRON
2459242.85953	7.67	1.24	CHIRON
2459245.72902	6.50	1.23	CHIRON
2459249.75002	7.22	0.95	CHIRON
2459252.75938	8.06	0.88	CHIRON
2459253.73586	8.85	0.87	CHIRON
2459255.78413	7.71	1.00	CHIRON
2459257.04496	12.33	1.31	MINERVA-AUS
2459258.73708	8.46	0.91	CHIRON
2459261.21232	9.00	0.89	MINERVA-AUS
2459267.28583	10.59	1.19	MINERVA-AUS
2459278.65059	7.59	0.98	CHIRON
2459301.12396	9.06	1.12	MINERVA-AUS
2460310.79654	-7.12	0.25	FEROS
2460312.77626	-6.98	0.29	FEROS
2459315.96764	11.98	1.53	MINERVA-AUS
2459323.94920	9.87	1.01	MINERVA-AUS
2459328.46905	7.18	1.17	CHIRON
2459328.76576	7.77	1.57	CHIRON
2459331.92638	7.87	0.85	MINERVA-AUS
2459344.91279	11.27	0.94	MINERVA-AUS
2459348.04569	8.75	0.77	MINERVA-AUS
2459349.99132	9.62	0.89	MINERVA-AUS
2459372.97197	9.05	1.10	MINERVA-AUS
2459988.71106	8.77	1.30	CHIRON
2459989.71543	9.30	1.10	CHIRON
2459990.72537	8.14	1.75	CHIRON
2459991.72212	9.74	1.53	CHIRON
2459992.75463	9.53	1.63	CHIRON
2459997.68743	10.13	1.15	CHIRON
2459998.69250	9.33	0.92	CHIRON
2459999.71994	9.93	1.91	CHIRON
2460000.71447	10.03	1.39	CHIRON
2460041.60773	8.94	1.99	CHIRON
2460042.64769	8.86	1.15	CHIRON
2460043.62817	10.02	1.09	CHIRON
2460049.63675	8.16	0.88	CHIRON
2460050.58596	9.18	1.02	CHIRON
2460051.60215	9.35	1.18	CHIRON
2460052.59233	9.95	0.99	CHIRON

2.2.3. MINERVA-Australis

MINERVA-Australis is an array of telescopes located at Mt Kent Observatory, Australia. It includes four identical 0.7 m telescopes feeding into one Kiwispec echelle spectrograph (Addison et al. 2019). Eleven observations for TOI-2005 were performed between February and July 2021. Radial velocities were derived using the least-squares deconvolution fit from each telescope individually. The velocities were weighted and combined after removing a fitted-for offset between each telescope. The combined velocities are presented in Table 2.

2.2.4. Transit Spectroscopic Observation

Spectroscopic observations were obtained during transit to measure the projected spin-orbit angle of the system. This technique is based on a phenomenon called the Rossiter-McLaughlin or RM effect (Rossiter 1924; McLaughlin 1924), in which the partial blockage of the rotating stellar surface by the transiting planet produces a distortion in the star’s spectral absorption lines. For example, when the planet is projected in front of the receding half of the star, some of the redshifted components of the line profiles are missing, and the overall line profile appears to be blueshifted.

The Magellan Inamori Kyocera Echelle (MIKE) spectrograph (Bernstein et al. 2003) on the Magellan Telescope at Las Campanas Observatory (LCO) in Chile was used to obtain simultaneous data with the blue (320-480 nm) and red (440-1000 nm) channels of the spectrograph on the night of 2023 Feb 27. Using a 0.35 arcsecond slit, MIKE-blue has a resolving power of $R = 83,000$ and MIKE-red has a resolving power of $R = 65,000$. Observations were acquired in sets of six 600-second observations alternating between the blue and red channels. Two Thorium-Argon calibration spectra were obtained between every set of observation. Calibrations and spectral extraction via the CARPY package (Kelson et al. 2000; Kelson 2003). The seeing was variable but mostly better than 1 arcsecond during the observations.

The Doppler shadow is extracted by deriving the line broadening profile using a least squares deconvolution between the observed spectra and a synthetic stellar template spectrum. The template spectrum was based on ATLAS9 (Castelli & Kurucz 2004) and was generated based on the estimated atmospheric parameters of the host star, with no rotational broadening incorporated. The portion of the star blocked by the transiting planet is modeled by the difference between the derived line profile and the median combined line profile, as described in Zhou et al. (2019). The analysis incorporates the effects of local limb darkening, macroturbulent broadening, and rotation. The line profile residuals for each transit observation, and for the combined observations, are shown in Figure 5. The light trail from bottom left to top

right represents the shadow of the planet during the transit in the line profile residuals.

The Doppler analysis was checked using two independent pipelines. In the first approach, we performed a joint fit of the TESS photometry and the Doppler shadow. Each TESS transit was modeled with a standard transit model plus a Gaussian Process model, described by the Matérn 3/2 kernel, for the treatment of correlated noise. For the Doppler shadow modeling, we first calculated the planet’s position on the stellar disk, and the corresponding stellar rotation velocity being blocked from view. We then convolved this “subplanet spectrum” with a Gaussian velocity profile. The width of the Gaussian profile was an adjustable parameter that depends on the resolution of the spectrograph and the macroturbulence of the star. Lastly, we calculated the likelihood by comparing the normalized planetary velocity profile at each time with the observed Doppler shadow. A detailed description of the model is provided in Section 4.2 of [Dong et al. \(2022\)](#). The model is built using the `exoplanet` and `PyMC` packages. After optimizing to determine the initial point for the Markov Chain Monte Carlo (MCMC), we ran 4 chains, each with 5000 tuning steps and 3000 draws. A target acceptance rate of 0.95 was used to avoid divergences.

We also performed a full global analysis using all available photometric and spectroscopic data as described in Section 3 and adopted the results as our final parameters as shown in Table 4.

2.3. SED analysis

We used all available broadband photometry, including *Hipparcos* *B* and *V* bands ([Perryman et al. 1997](#)), *Gaia* DR3 *G*, *B_p*, *R_p* ([Gaia Collaboration et al. 2022a](#)), 2MASS *J*, *H*, *K* ([Skrutskie et al. 2006](#)), and WISE *W₁*, *W₂*, *W₃*, *W₄* bands ([Cutri et al. 2021a](#)), as well as *Gaia* DR3 parallaxes to construct the spectral energy distribution of TOI-2005. The spectral energy distribution was modeled simultaneously with the photometric and spectroscopic observations of the system which is discussed in the next Section. The best-fit model is shown in Figure 6 and the catalog parameters are reported in Table 3.

3. GLOBAL MODELING

We performed a joint analysis of all available photometric, spectroscopic, and catalog observations to determine the stellar and planetary parameters of the system. This included photometric transit observations from TESS and follow-up ground-based observatories (Section 2.1.1 and 2.1.2), a spectroscopic transit observation from MIKE (Section 2.2.4), and radial velocities from CHIRON, FEROS, and MINERVA-Australis (Section 2.2). Free parameters largely describing the transit include the orbital period *P*, reference time of transit center *T₀*, planet-to-star radius ratio *R_p/R_∗*, line-of-sight

Table 3. Literature values for TOI-2005.

Stellar Parameters	Value	Source
Catalog Information		
TIC ID	147660886	TOI Catalog
TOI ID	2005	TOI Catalog
<i>Gaia</i> DR3 ID	5388416255319817856	GAIA DR3
2MASS ID	J10560763-4322362	2MASS
TYC ID	7736-00803-1	Tycho
Coordinates and Proper Motion		
Right Ascension (h:m:s)	10:56:07.60 (J2000)	GAIA DR3
Declination (d:m:s)	-43:22:36.1 (J2000)	GAIA DR3
Parallax (mas)	2.991 ± 0.017	GAIA DR3
μ_{RA} (mas yr ⁻¹)	-25.248 ± 0.012	GAIA DR3
μ_{Dec} (mas yr ⁻¹)	8.399 ± 0.016	GAIA DR3
Magnitudes		
<i>TESS</i> (mag)	9.492 ± 0.006	TOI Catalog
<i>G</i> (mag)	9.76491 ± 0.00013	GAIA DR3
<i>B_p</i> (mag)	9.95198 ± 0.00018	GAIA DR3
<i>R_p</i> (mag)	9.43687 ± 0.00017	GAIA DR3
<i>B</i> (mag)	10.222 ± 0.049	Tycho
<i>V</i> (mag)	9.867 ± 0.003	Tycho
<i>J</i> (mag)	9.099 ± 0.034	2MASS
<i>H</i> (mag)	8.977 ± 0.023	2MASS
<i>K</i> (mag)	8.905 ± 0.019	2MASS
<i>WISE</i> _{3.4μ} (mag)	8.863 ± 0.022	WISE
<i>WISE</i> _{4.6μ} (mag)	8.882 ± 0.020	WISE
<i>WISE</i> _{12μ} (mag)	8.846 ± 0.026	WISE
<i>WISE</i> _{22μ} (mag)	8.663 ± 0.348	WISE

Note: TESS TOI Primary Mission Catalog; ([Guerrero et al. 2021](#)), Tycho; ([Høg et al. 2000](#)); GAIA DR3; ([Gaia Collaboration et al. 2022b](#)), 2MASS; ([Cutri et al. 2003](#)), WISE; ([Cutri et al. 2021b](#))

inclination *i*, and orbital eccentricity parameters $\sqrt{e} \cos \omega$ and $\sqrt{e} \sin \omega$ where *e* is the orbital eccentricity and ω the argument of periastron. In addition, the radial velocity orbit and spectroscopic transits are described by the mass of the planetary companion *M_p* and its projected orbital obliquity λ . Simultaneous with the transit models, we also interpolated the stellar isochrones as per Section 2.3. At each step, we modeled the spectral energy distribution to constrain the stellar parameters. Free parameters describing the stellar isochrone and spectral energy distribution modeling include stellar mass *M_∗*, age, metallicity [m/H], and parallax. Parallax is tightly constrained by a Gaussian prior about its *Gaia* DR3 value and associated uncertainties. We also include free parameters for the rotational and macroturbulent velocities to enable modeling of the spectroscopic transits. These values are also tightly constrained by their spectroscopic measurements and associated uncertainties.

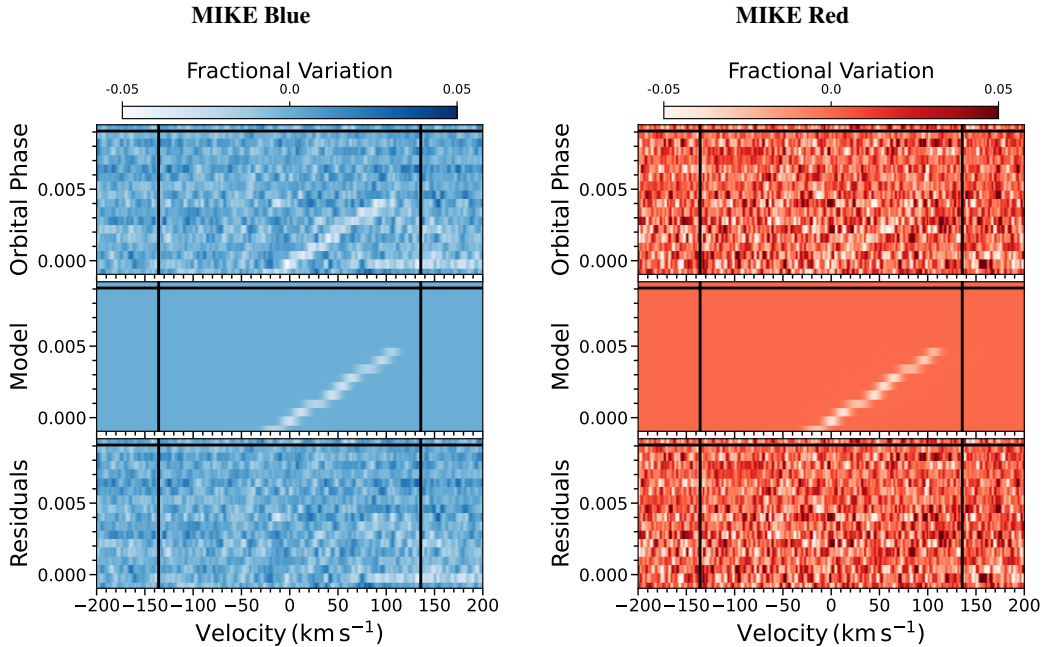


Figure 5. MIKE Doppler spectroscopic results from February 27, 2023. The color scale represents the fractional variation in the spectral line profile. Each plot shows the planetary signal after the average rotational profile is subtracted (top), the best-fit model (middle), and the residuals after subtracting the planetary signal (bottom).

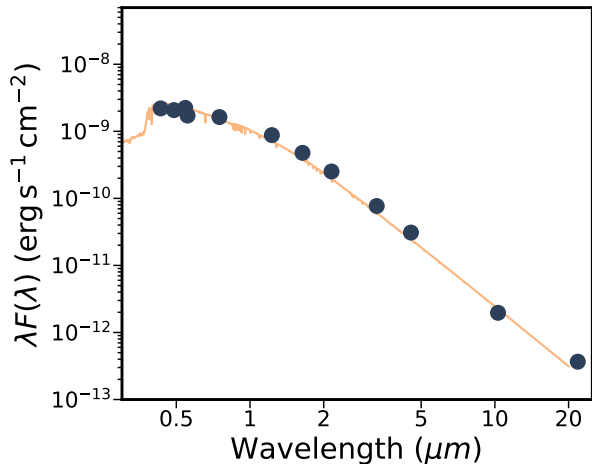


Figure 6. Spectral energy distribution of the target star TOI-2005. Magnitudes from *Gaia* G , B_p , R_p , *Tycho* B , V , 2MASS J , H , K_s , and WISE $W1$, $W2$, $W3$, and $W4$ are included in the global modeling of the system and are shown in dark blue.

The photometric transits are modeled as per Mandel & Agol (2002) via the BATMAN package (Kreidberg 2015). Limb darkening parameters are interpolated and fixed to their values as per Claret & Bloemen (2011), Claret (2017) and Eastman et al. (2013). The spectroscopic transit is modeled as per Section 2.2.4, via a disk integration of the portion of the stellar surface occulted by the planet, incorporating the

effect of local macroturbulence and rotational broadening. The best fit parameters are presented in Table 3 and Table 4.

4. DISCUSSION

TOI-2005 b is a warm Jupiter with an orbital period of 17.3 days. We were unable to detect an orbital signal due to the rapid rotation of the host star, but we have placed a 3σ upper limit on the planet mass of $6.4 M_{\text{Jup}}$ and determined that the object is planetary in nature. The planet orbits an early F-type star ($T_{\text{eff}} = 7130 \pm 150$ K) with a mass of $1.59 M_{\odot}$ and a radius of $2.02^{+0.14}_{-0.16} R_{\odot}$. The planet orbits the host star in an eccentric orbit determined to be $0.597^{+0.097}_{-0.065}$ with a measured sky-projected spin-orbit angle of $\lambda = 4.8^{+2.3}_{-2.5}$ deg.

4.1. High eccentricity coplanar migration

The highly eccentric nature of TOI-2005 b is determined via a joint modeling of the photometric transit and the radial velocity orbit. The stellar parameters are well constrained by the spectral energy distribution and *Gaia* parallax, providing a constrained stellar mass and radius. The short transit duration of TOI-2005 b, compared to that expected for a circular orbit, is indicative that the transit is occurring at periastron passage. Higher eccentricity solutions are constrained by the lack of a radial velocity detection at periastron. The posterior distribution for eccentricity against relevant parameters that influence its value and precision are shown in Figure 7 for reference.

Table 4. Best-fit Stellar and Planetary Properties for TOI-2005

Parameters	Description (Units)	Prior Values	Best Fit
Stellar Parameters:			
M_*	Stellar Mass (M_\odot)	$\mathcal{U}(1, 3)$	$1.59^{+0.016}_{-0.017}$
R_*	Stellar Radius (R_\odot)	Inferred	$2.02^{+0.14}_{-0.16}$
L_*	Stellar Luminosity (L_\odot)	Inferred	$9.17^{+0.52}_{-0.99}$
T_{eff}	Effective Temperature (K)	Inferred	7130 ± 150
$\log g$	Surface Gravity (cgs)	Inferred	3.946 ± 0.035
[m/H]	Metallicity (dex)	Fixed	0
$v \sin i$	Projected Rotational Velocity (km s^{-1})	$\mathcal{G}(110, 1.0)$	111 ± 1
v_{macro}	Macroturbulent velocity (km s^{-1})	$\mathcal{U}(0, 20)$	3.7 ± 1.6
Parallax	Parallax (mas)	$\mathcal{G}(11.409, 0.026)$	11.409 ± 0.025
Age	Age (Gyr)	$\mathcal{U}(0.1, 2.0)$	1.6 ± 0.1
Distance	Distance (pc)	Inferred	$328.7^{+4.6}_{-4.2}$
$E(B - V)$	Reddening (mag)	Inferred	$0.012^{+0.013}_{-0.009}$
Planetary Parameters:			
P	Orbital Period (days)	$\mathcal{U}(17.2, 17.4)$	$17.305904^{+0.000023}_{-0.000020}$
T_o	Epoch (BJD)	$\mathcal{U}(2458549.8, 2458549.9)$	$2458549.8376^{+0.0011}_{-0.0013}$
M_p	Planet Mass (M_{Jup})	$\mathcal{U}(0, 100)$	$< 6.4 (3\sigma)$
R_p	Planet Radius (R_{Jup})	Inferred	$1.07^{+0.06}_{-0.11}$
R_p/R_*	Radius of planet to star ratio	$\mathcal{U}(0.03, 0.10)$	$0.05107^{+0.00037}_{-0.00045}$
a/R_*	Semi-major axis to star radius ratio	Inferred	$15.9^{+1.97}_{-1.75}$
a	Semi-major axis (AU)	Inferred	0.16 ± 0.02
e	eccentricity	Inferred	$0.597^{+0.097}_{-0.065}$
$\sqrt{e} \cos \omega$	eccentricity parameter	$\mathcal{U}(-1, 1)^a$	$-0.254^{+0.065}_{-0.078}$
$\sqrt{e} \sin \omega$	eccentricity parameter	$\mathcal{U}(-1, 1)^a$	$0.729^{+0.024}_{-0.040}$
γ	Radial velocity offset (km s^{-1})	$\mathcal{U}(24, 25)$	$24.424^{+0.077}_{-0.072}$
T_{14}	Transit duration (hours)	Inferred	2.249 ± 0.063
K	RV semi-amplitude (m/s)	Inferred	$< 1320 (3\sigma)$
i	Transit inclination (deg)	$\mathcal{U}(80, 90.5)^a$	$87.1^{+1.1}_{-0.9}$
b	Impact parameter	Inferred	$0.52^{+0.33}_{-0.35}$
λ	Projected Spin-Orbit Angle (deg)	$\mathcal{U}(0, 180)$	$4.8^{+2.3}_{-2.5}$

^aParameters that result in $e > 1$ or non-transiting solutions are excluded within the MCMC.

Note: Inferred parameters are not directly modeled but are derived from other parameters.

TOI-2005 b might be undergoing high-eccentricity tidal migration as inferred from the semi-major axis and eccentricity, and shown in Figure 8. TOI-2005 b currently resides at a semi-major axis of 0.16 ± 0.02 au but as the planet passes through periastron on its eccentric orbit, energy dissipation interior to the planet will lead to tidal circularization. The planet has an eccentricity of $0.597^{+0.097}_{-0.065}$ and a semi-major axis (a_p) of 0.16 ± 0.02 au. If its orbit can be circularized within the life of the planetary system, it will end up with an orbital distance of 0.101 au, as defined by $a_{\text{final}} = a(1 - e^2)$ following the evolution of constant angular momentum tracks (see Dawson & Johnson (2018) for a review). The timescale for tidal circularization varies and

relies heavily on the quality dissipation parameter, Q'_p . If we calculate the tidal circularization for the system (Equation 1) adopted from Adams & Laughlin (2006) while assuming a $Q'_p = 10^6$, we calculate that the circularization timescale of the planet is $\sim 10^{11}$ years and much longer than the age of the system.

$$\tau_{\text{circ}} \sim \frac{4Q'_p}{63} \left(\frac{a}{GM_*}\right)^{1/2} \frac{M_p}{M_*} \left(\frac{a}{R_p}\right)^5 (1 - e^2)^{13/2} [F(e^2)]^{-1} \quad (1)$$

We note that the circularization timescale would change depending on what Q'_p value is adopted and that Q'_p does not stay constant during the planet's evolution.

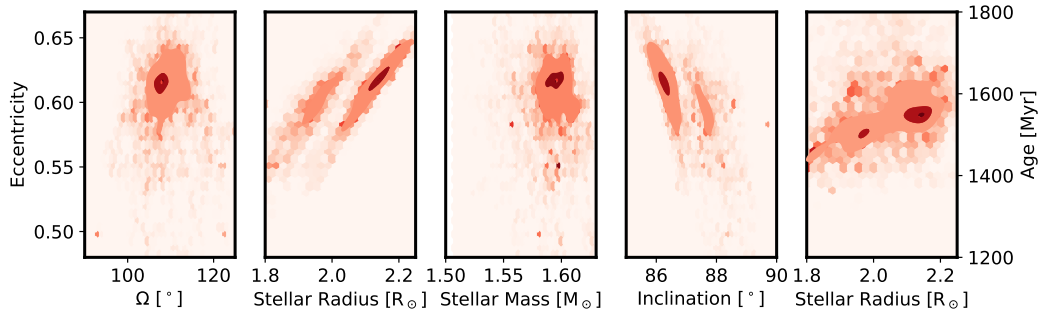


Figure 7. Correlations between eccentricity and key parameters that affect its posterior distribution, including the argument of periastron Ω , stellar mass and radius, and transit inclination. The 1σ and 2σ regions are marked by the red 2D histograms. We note a bimodality in the stellar radius as the posterior overlaps between the main sequence and subgiant branches.

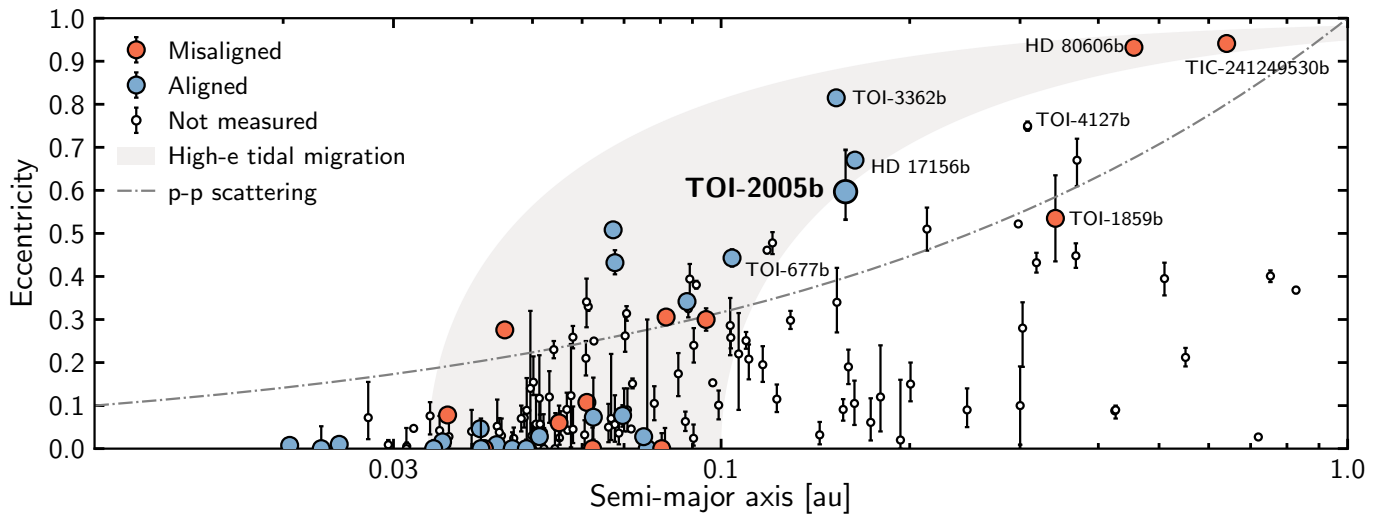


Figure 8. Eccentricity vs. semi-major axis for all confirmed transiting planets between 6–20 Earth radii. Colored circles are planets with measured spin-orbit angles. Blue circles are defined as ‘aligned’ with spin-orbit angles of less than 30 degrees and red circles are defined as ‘misaligned’ with spin-orbit angles greater than 30 degrees. The gray region illustrates planets that are likely undergoing high-eccentricity tidal migration. The upper and lower limits of the track are set by the Roche limit and the tidal circularization timescale (Dong et al. 2021). TOI-2005 b sits on the lower edge of the migration track. The dotted-dashed line presents the theoretical upper limit of eccentricities as a result of planet-planet scattering, assuming a planet with a mass of $0.5 M_{\text{Jup}}$ and a radius of $2 R_{\text{Jup}}$, for illustrative purpose (Petrovich et al. 2014). Data were compiled from the NASA Exoplanet Archive as of October 30, 2024. Stellar obliquity measurements were obtained from Knudstrup et al. (2024) Table B2 with recent updates.

Most high eccentricity migration mechanisms result in a wide range of final orbital obliquities (see summaries in Albrecht et al. 2022). One mechanism for hot Jupiters existing with high eccentricity and low obliquity is explained through Coplanar High-Eccentricity Migration (Petrovich 2015). In this scenario, a coplanar inner Jovian planet is formed via secular interactions between it and another giant planet much farther out at low mutual inclinations. The farther out companion would be difficult to detect given the long period, the small RV signal, and the host star’s rotational velocity. We do not detect any additional bodies in our current dataset. Coplanar high-eccentricity migration is applicable to some outcomes of prior planet-planet scattering events that result in high eccentricity orbits for both the inner and outer planet at

low mutual inclinations (Timpe et al. 2013). Coplanar high-eccentricity migration then acts to migrate the inner Jovian planet inward via high eccentricity and tidal circularization, while keeping the mutual inclination of the two planets low. In many cases, this also results in the formation of a coplanar, low obliquity hot Jupiter. Another method for generating low or moderately eccentric Jupiters is through disk-driven migration. Typically disk-driven migration is thought to be a smooth migration mechanism but if the planet migrates into a low-density disk cavity, the eccentricity can increase due to resonances and will not be opposed given the lack of gas in the cavity (Debras et al. 2021; Li & Lai 2023).

The discovery of low-obliquity, eccentric warm Jupiters can help trace the prevalence of this migration pathway. Pre-

vious examples include HD 17156 b (Fischer et al. 2007; Barbieri et al. 2009), TOI-3362 b (Dong et al. 2021; Espinoza-Retamal et al. 2023b), HD 118203 b (Pepper et al. 2020; Zhang et al. 2024), and TOI-677 b (Jordán et al. 2020b; Sedaghati et al. 2023). In fact, of the eight planets with obliquities measured that are clearly within the high-eccentricity evolution track, and exhibit modest eccentricities larger than that predicted by planet-planet scattering (see the dotted-dashed line in Figure 8), six have low projected obliquities. Assuming these projected obliquities are representative of their true 3D obliquities, their predominance is a clue that co-planar migration plays an important role in the formation of hot Jupiters.

4.2. Atmospheric circulation in a highly eccentric orbit

The level of stellar irradiation received by TOI-2005 b changes by more than an order of magnitude in less than 10 days. Unlike most circularized hot Jupiters, TOI-2005 b is not expected to have a constant day/night side. To understand how this change in irradiation might affect such a planet we perform atmospheric modeling using *EGP+*, a 1D time-stepping radiative-convective equilibrium model (Mayorga et al. 2021). We follow the approach laid out in Mayorga et al. (2021) to initialize the model and ensure spin up using the assumptions of Solar metallicity, C/O ratio, and a cloud-free atmosphere. In Figure 9, we show how the model atmosphere’s temperature varies as a function of pressure and orbital phase. Near periastron, the presence of TiO and VO cause a rapid change in the upper atmospheric temperatures leading to a predicted inversion in the planet’s TP profile. The planetary equilibrium temperature fluctuates from a maximum temperature of 2171 K just after periastron passage at phase 0.01 to a minimum temperature of 1217 K at phase -0.38. In Figure 10, we show how the model atmosphere’s planet-to-star flux ratio varies as a function of orbital phase. Near apastron where the model atmosphere is relatively cool, many species have absorption features which shape the spectrum. As the planet transitions towards periastron, it passes through a blackbody phase before progressing to the near periastron state where signatures from water and carbon monoxide are the only features that remain due to the inverted nature and temperature of the TP profile.

Ultra-Hot Jupiters with similar equilibrium temperatures have neutral and ionized atomic species detected via high-resolution spectroscopic cross-correlations (e.g. KELT-20b/MASCARA-2 b, (Hoeijmakers et al. 2020a; Johnson et al. 2023; Singh et al. 2024) and WASP-121 b (Hoeijmakers et al. 2020b,c; Casasayas-Barris et al. 2022)). All of these previous planets reside in near-circular orbits, and receive near-constant stellar irradiation. The only existing measurements of rapid heating of exoplanet atmospheres were done in the infrared for HD 80606 b ($e = 0.93$) (Sikora et al. 2024)

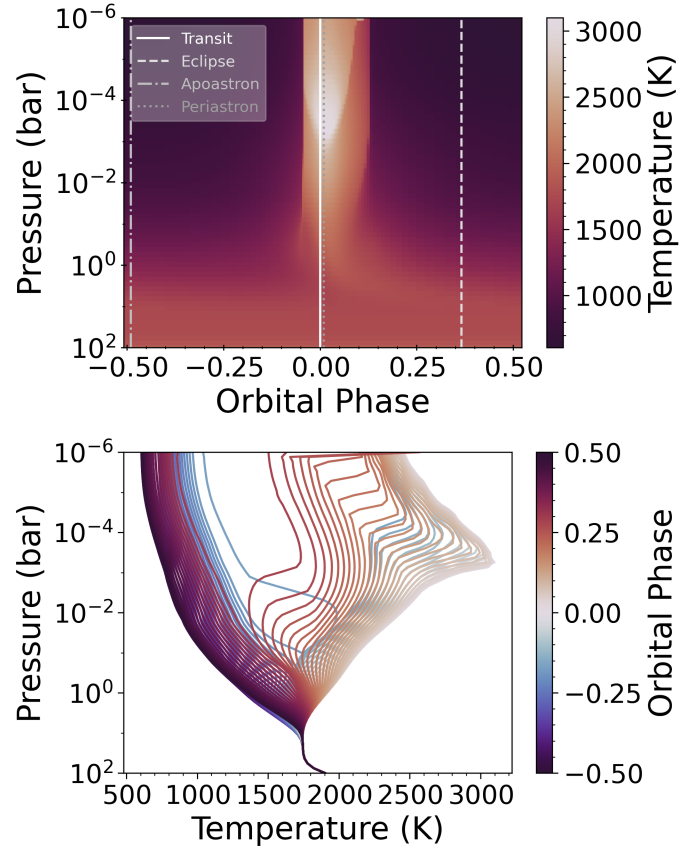


Figure 9. Temperature as a function of pressure over orbital phase from a 1D timestepping cloud-free atmospheric model generated using *EGP+*. Due to the presence of TiO and VO in the model atmosphere, at periastron the temperature of the upper atmosphere rises rapidly causing an inversion.

and HAT-P-2 b ($e = 0.5$) (Laughlin et al. 2009; Lewis et al. 2013)) and both found extremely short atmospheric radiative time scales compared to Solar System planets. By comparing the strength of neutral and ionized species in the atmosphere of TOI-2005 b, which undergoes these orbital induced thermal pulses, against those detected for planets in circular orbits, we can constrain the specific timescales of the chemical transitions and element transporting that take place in its highly irradiated atmospheres (Mayorga et al. 2021). These time scales are crucial inputs for exoplanetary global circulation models (Lewis et al. 2013), which would impact our deeper understanding of high signal-to-noise spectroscopic observations of exoplanetary atmospheres.

ACKNOWLEDGMENTS

We respectfully acknowledge the traditional custodians of the lands on which we conducted this research and throughout Australia. We recognize their continued cultural and spiritual connection to the land, waterways, cosmos and community. We pay our deepest respects to all Elders, present and emerging people of the Giabal, Jarowair

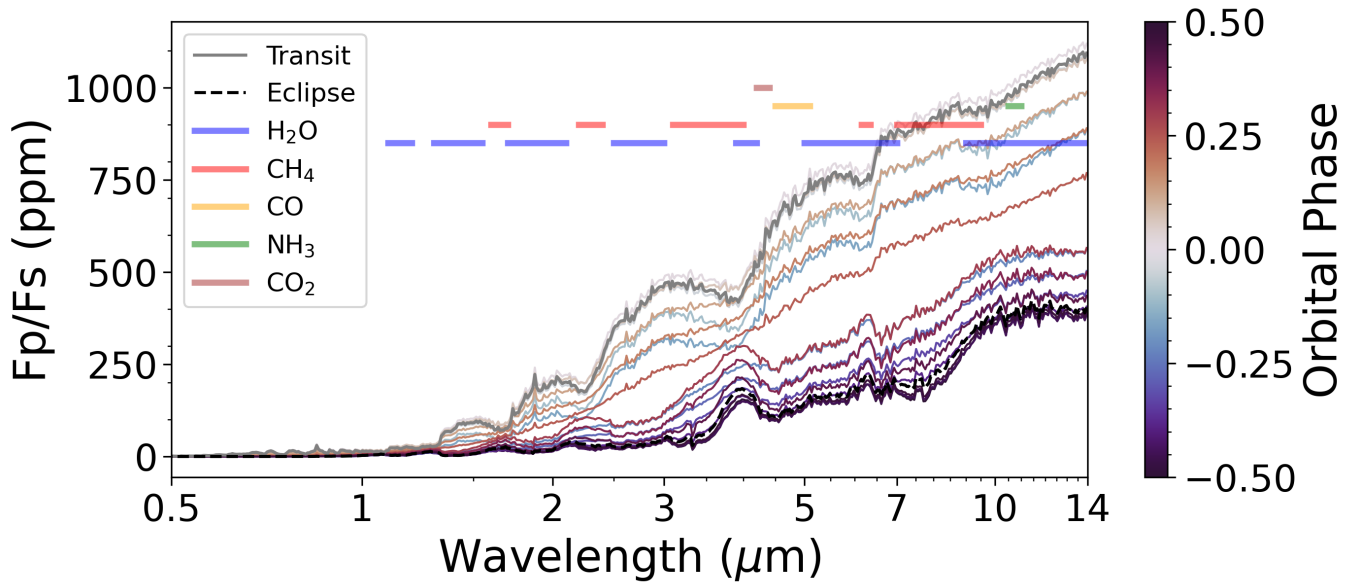


Figure 10. Planet-to-star flux ratio as a function of orbital phase from the same model as Figure 9. At apastron the spectra show many species in absorption (colored bars) and as the planet progresses towards periastron only the CO feature remains (in emission) with water providing the bulk of the increase in flux from a blackbody due to being in emission.

and Kambuwal nations, upon whose lands this research was conducted. CH thanks the support of the ARC DECRA program DE200101840 and Future Fellowship program FT240100016. GZ thanks the support of the ARC DECRA program DE210101893 and Future Fellowship program FT230100517. Funding for the TESS mission is provided by NASA’s Science Mission Directorate. We acknowledge the use of public TESS data from pipelines at the TESS Science Office and at the TESS Science Processing Operations Center. This research has made use of the Exoplanet Follow-up Observing Program website, which is operated by the California Institute of Technology, under contract with the National Aeronautics and Space Administration under the Exoplanet Exploration Program. Resources supporting this work were provided by the NASA High-End Computing (HEC) Program through the NASA Advanced Supercomputing (NAS) Division at Ames Research Center for the production of the SPOC data products. This paper includes data collected by the TESS mission that are publicly available from the Mikulski Archive for Space Telescopes (MAST). This work has made use of data from the European Space Agency (ESA) mission *Gaia* (<https://www.cosmos.esa.int/gaia>), processed by the *Gaia* Data Processing and Analysis Consortium (DPAC, <https://www.cosmos.esa.int/web/gaia/dpac/consortium>). Funding for the DPAC has been provided by national institutions, in particular the institutions participating in the *Gaia* Multilateral Agreement. The Flatiron Institute is

a division of the Simons foundation. This work makes use of observations from the LCOGT network. Part of the LCOGT telescope time was granted by NOIRLab through the Mid-Scale Innovations Program (MSIP). MSIP is funded by NSF. This work makes use of observations from the ASTEP telescope. ASTEP benefited from the support of the French and Italian polar agencies IPEV and PNRA in the framework of the Concordia station program and from OCA, INSU, Idex UCAJEDI (ANR- 15-IDEX-01) and ESA through the Science Faculty of the European Space Research and Technology Centre (ESTEC). This research also received funding from the European Research Council (ERC) under the European Union’s Horizon 2020 research and innovation program (grant agreement No. 803193/BEBOP) and from the Science and Technology Facilities Council (STFC; grant No. ST/S00193X/1). A.J. acknowledges support from ANID – Millennium Science Initiative – ICN12.009, AIM23-0001 and from FONDECYT project 1210718.

Facilities: MAST(TESS), CHIRON, FEROS, MINERVA-AUS, ASTEP, LCO, SOAR, ExoFOP

Software: AstroImageJ (Collins et al. 2017), Lightkurve (Lightkurve Collaboration et al. 2018), Tapir (Jensen 2013), Batman (Kreidberg 2015)

REFERENCES

- Abe, L., Gonçalves, I., Agabi, A., et al. 2013, *A&A*, 553, A49, doi: [10.1051/0004-6361/201220351](https://doi.org/10.1051/0004-6361/201220351)
- Adams, F. C., & Laughlin, G. 2006, *ApJ*, 649, 1004, doi: [10.1086/506145](https://doi.org/10.1086/506145)

- Addison, B., Wright, D. J., Wittenmyer, R. A., et al. 2019, *PASP*, 131, 115003, doi: [10.1088/1538-3873/ab03aa](https://doi.org/10.1088/1538-3873/ab03aa)
- Albrecht, S. H., Dawson, R. I., & Winn, J. N. 2022, *PASP*, 134, 082001, doi: [10.1088/1538-3873/ac6c09](https://doi.org/10.1088/1538-3873/ac6c09)
- Barbieri, M., Alonso, R., Desidera, S., et al. 2009, *A&A*, 503, 601, doi: [10.1051/0004-6361/200811466](https://doi.org/10.1051/0004-6361/200811466)
- Bernstein, R., Shtetman, S. A., Gunnels, S. M., Mochnecki, S., & Athey, A. E. 2003, in *Society of Photo-Optical Instrumentation Engineers (SPIE) Conference Series*, Vol. 4841, *Instrument Design and Performance for Optical/Infrared Ground-based Telescopes*, ed. M. Iye & A. F. M. Moorwood, 1694–1704, doi: [10.1117/12.461502](https://doi.org/10.1117/12.461502)
- Brahm, R., Jordán, A., & Espinoza, N. 2017, *Publications of the Astronomical Society of the Pacific*, 129, 034002, doi: [10.1088/1538-3873/aa5455](https://doi.org/10.1088/1538-3873/aa5455)
- Brahm, R., Espinoza, N., Jordán, A., et al. 2019, *AJ*, 158, 45, doi: [10.3847/1538-3881/ab279a](https://doi.org/10.3847/1538-3881/ab279a)
- Brown, T. M., Baliber, N., Bianco, F. B., et al. 2013, *PASP*, 125, 1031, doi: [10.1086/673168](https://doi.org/10.1086/673168)
- Caldwell, D. A., Tenenbaum, P., Twicken, J. D., et al. 2020, *Research Notes of the American Astronomical Society*, 4, 201, doi: [10.3847/2515-5172/abc9b3](https://doi.org/10.3847/2515-5172/abc9b3)
- Casasayas-Barris, N., Borsa, F., Palle, E., et al. 2022, *A&A*, 664, A121, doi: [10.1051/0004-6361/202143016](https://doi.org/10.1051/0004-6361/202143016)
- Castelli, F., & Kurucz, R. L. 2004, *ArXiv Astrophysics e-prints*
- Chatterjee, S., Ford, E. B., Matsumura, S., & Rasio, F. A. 2008, *ApJ*, 686, 580, doi: [10.1086/590227](https://doi.org/10.1086/590227)
- Claret, A. 2017, *A&A*, 600, A30, doi: [10.1051/0004-6361/201629705](https://doi.org/10.1051/0004-6361/201629705)
- Claret, A., & Bloemen, S. 2011, *A&A*, 529, A75, doi: [10.1051/0004-6361/201116451](https://doi.org/10.1051/0004-6361/201116451)
- Clemens, J. C., Crain, J. A., & Anderson, R. 2004, in *Society of Photo-Optical Instrumentation Engineers (SPIE) Conference Series*, Vol. 5492, *Ground-based Instrumentation for Astronomy*, ed. A. F. M. Moorwood & M. Iye, 331–340, doi: [10.1117/12.550069](https://doi.org/10.1117/12.550069)
- Collins, K. 2019, in *American Astronomical Society Meeting Abstracts*, Vol. 233, *American Astronomical Society Meeting Abstracts #233*, 140.05
- Collins, K. A., Kielkopf, J. F., Stassun, K. G., & Hessman, F. V. 2017, *AJ*, 153, 77, doi: [10.3847/1538-3881/153/2/77](https://doi.org/10.3847/1538-3881/153/2/77)
- Cutri, R. M., Skrutskie, M. F., van Dyk, S., et al. 2003, *VizieR Online Data Catalog*, II/246
- Cutri, R. M., Wright, E. L., Conrow, T., et al. 2021a, *VizieR Online Data Catalog*, II/328
- . 2021b, *VizieR Online Data Catalog*, II/328
- Dawson, R. I., & Johnson, J. A. 2018, *ARA&A*, 56, 175, doi: [10.1146/annurev-astro-081817-051853](https://doi.org/10.1146/annurev-astro-081817-051853)
- Debras, F., Baruteau, C., & Donati, J.-F. 2021, *MNRAS*, 500, 1621, doi: [10.1093/mnras/staa3397](https://doi.org/10.1093/mnras/staa3397)
- Dong, J., Huang, C. X., Zhou, G., et al. 2021, *ApJL*, 920, L16, doi: [10.3847/2041-8213/ac2600](https://doi.org/10.3847/2041-8213/ac2600)
- . 2022, *ApJL*, 926, L7, doi: [10.3847/2041-8213/ac4da0](https://doi.org/10.3847/2041-8213/ac4da0)
- Dong, J., Wang, S., Rice, M., et al. 2023, *ApJL*, 951, L29, doi: [10.3847/2041-8213/acd93d](https://doi.org/10.3847/2041-8213/acd93d)
- Eastman, J., Gaudi, B. S., & Agol, E. 2013, *PASP*, 125, 83, doi: [10.1086/669497](https://doi.org/10.1086/669497)
- Espinoza-Retamal, J. I., Brahm, R., Petrovich, C., et al. 2023a, *ApJL*, 958, L20, doi: [10.3847/2041-8213/ad096d](https://doi.org/10.3847/2041-8213/ad096d)
- . 2023b, *ApJL*, 958, L20, doi: [10.3847/2041-8213/ad096d](https://doi.org/10.3847/2041-8213/ad096d)
- Fischer, D. A., Vogt, S. S., Marcy, G. W., et al. 2007, *ApJ*, 669, 1336, doi: [10.1086/521869](https://doi.org/10.1086/521869)
- Gaia Collaboration, Vallenari, A., Brown, A. G. A., et al. 2022a, *arXiv e-prints*, arXiv:2208.00211, doi: [10.48550/arXiv.2208.00211](https://doi.org/10.48550/arXiv.2208.00211)
- . 2022b, *arXiv e-prints*, arXiv:2208.00211, doi: [10.48550/arXiv.2208.00211](https://doi.org/10.48550/arXiv.2208.00211)
- Gray, D. F. 2005, *The Observation and Analysis of Stellar Photospheres* (Cambridge University Press)
- Guerrero, N. M., Seager, S., Huang, C. X., et al. 2021, *ApJS*, 254, 39, doi: [10.3847/1538-4365/abefe1](https://doi.org/10.3847/1538-4365/abefe1)
- Guillot, T., Abe, L., Agabi, A., et al. 2015, *Astronomische Nachrichten*, 336, 638, doi: [10.1002/asna.201512174](https://doi.org/10.1002/asna.201512174)
- Hobson, M. J., Trifonov, T., Henning, T., et al. 2023, *AJ*, 166, 201, doi: [10.3847/1538-3881/acfc1d](https://doi.org/10.3847/1538-3881/acfc1d)
- Hoeijmakers, H. J., Cabot, S. H. C., Zhao, L., et al. 2020a, *A&A*, 641, A120, doi: [10.1051/0004-6361/202037437](https://doi.org/10.1051/0004-6361/202037437)
- . 2020b, *A&A*, 641, A120, doi: [10.1051/0004-6361/202037437](https://doi.org/10.1051/0004-6361/202037437)
- Hoeijmakers, H. J., Seidel, J. V., Pino, L., et al. 2020c, *A&A*, 641, A123, doi: [10.1051/0004-6361/202038365](https://doi.org/10.1051/0004-6361/202038365)
- Høg, E., Fabricius, C., Makarov, V. V., et al. 2000, *A&A*, 355, L27
- Huang, C. X., Vanderburg, A., Pál, A., et al. 2020, *Research Notes of the American Astronomical Society*, 4, 204, doi: [10.3847/2515-5172/abca2e](https://doi.org/10.3847/2515-5172/abca2e)
- Jenkins, J. M. 2002, *ApJ*, 575, 493, doi: [10.1086/341136](https://doi.org/10.1086/341136)
- Jenkins, J. M., Tenenbaum, P., Seader, S., et al. 2020, *Kepler Data Processing Handbook: Transiting Planet Search*, *Kepler Science Document KSCI-19081-003*, id. 9. Edited by Jon M. Jenkins.
- Jenkins, J. M., Chandrasekaran, H., McCauliff, S. D., et al. 2010, in *Society of Photo-Optical Instrumentation Engineers (SPIE) Conference Series*, Vol. 7740, *Software and Cyberinfrastructure for Astronomy*, ed. N. M. Radziwill & A. Bridger, 77400D, doi: [10.1117/12.856764](https://doi.org/10.1117/12.856764)
- Jenkins, J. M., Twicken, J. D., McCauliff, S., et al. 2016, in *Society of Photo-Optical Instrumentation Engineers (SPIE) Conference Series*, Vol. 9913, *Software and Cyberinfrastructure for Astronomy IV*, ed. G. Chiozzi & J. C. Guzman, 99133E, doi: [10.1117/12.2233418](https://doi.org/10.1117/12.2233418)

- Jensen, E. 2013, Tapir: A web interface for transit/eclipse observability, *Astrophysics Source Code Library*, record ascl:1306.007. <http://ascl.net/1306.007>
- Johnson, M. C., Wang, J., Asnodkar, A. P., et al. 2023, *AJ*, 165, 157, doi: [10.3847/1538-3881/acb7e2](https://doi.org/10.3847/1538-3881/acb7e2)
- Jones, M. I., Reinartz, Y., Brahm, R., et al. 2024, *A&A*, 683, A192, doi: [10.1051/0004-6361/202348147](https://doi.org/10.1051/0004-6361/202348147)
- Jordán, A., Brahm, R., Espinoza, N., et al. 2020a, *AJ*, 159, 145, doi: [10.3847/1538-3881/ab6f67](https://doi.org/10.3847/1538-3881/ab6f67)
- . 2020b, *AJ*, 159, 145, doi: [10.3847/1538-3881/ab6f67](https://doi.org/10.3847/1538-3881/ab6f67)
- Kaufer, A., Stahl, O., Tubbesing, S., et al. 1999, *The Messenger*, 95, 8
- Kelson, D. D. 2003, *PASP*, 115, 688, doi: [10.1086/375502](https://doi.org/10.1086/375502)
- Kelson, D. D., Illingworth, G. D., van Dokkum, P. G., & Franx, M. 2000, *ApJ*, 531, 137, doi: [10.1086/308460](https://doi.org/10.1086/308460)
- Knudstrup, E., Albrecht, S. H., Winn, J. N., et al. 2024, *A&A*, 690, A379, doi: [10.1051/0004-6361/202450627](https://doi.org/10.1051/0004-6361/202450627)
- Kovács, G., Zucker, S., & Mazeh, T. 2002, *A&A*, 391, 369, doi: [10.1051/0004-6361:20020802](https://doi.org/10.1051/0004-6361:20020802)
- Kozai, Y. 1962, *AJ*, 67, 591, doi: [10.1086/108790](https://doi.org/10.1086/108790)
- Kreidberg, L. 2015, *PASP*, 127, 1161, doi: [10.1086/683602](https://doi.org/10.1086/683602)
- Kunimoto, M., Tey, E., Fong, W., et al. 2022, *Research Notes of the American Astronomical Society*, 6, 236, doi: [10.3847/2515-5172/aca158](https://doi.org/10.3847/2515-5172/aca158)
- Laughlin, G., Deming, D., Langton, J., et al. 2009, *Nature*, 457, 562, doi: [10.1038/nature07649](https://doi.org/10.1038/nature07649)
- Lewis, N. K., Knutson, H. A., Showman, A. P., et al. 2013, *ApJ*, 766, 95, doi: [10.1088/0004-637X/766/2/95](https://doi.org/10.1088/0004-637X/766/2/95)
- Li, J., & Lai, D. 2023, *ApJ*, 956, 17, doi: [10.3847/1538-4357/aced89](https://doi.org/10.3847/1538-4357/aced89)
- Li, J., Tenenbaum, P., Twicken, J. D., et al. 2019, *PASP*, 131, 024506, doi: [10.1088/1538-3873/aaf44d](https://doi.org/10.1088/1538-3873/aaf44d)
- Lidov, M. L. 1962, *Planet. Space Sci.*, 9, 719, doi: [10.1016/0032-0633\(62\)90129-0](https://doi.org/10.1016/0032-0633(62)90129-0)
- Lightkurve Collaboration, Cardoso, J. V. d. M., Hedges, C., et al. 2018, *Lightkurve: Kepler and TESS time series analysis in Python*, *Astrophysics Source Code Library*. <http://ascl.net/1812.013>
- Mandel, K., & Agol, E. 2002, *ApJL*, 580, L171, doi: [10.1086/345520](https://doi.org/10.1086/345520)
- Mayorga, L. C., Robinson, T. D., Marley, M. S., May, E. M., & Stevenson, K. B. 2021, *ApJ*, 915, 41, doi: [10.3847/1538-4357/abff50](https://doi.org/10.3847/1538-4357/abff50)
- McCully, C., Volgenau, N. H., Harbeck, D.-R., et al. 2018, in *Society of Photo-Optical Instrumentation Engineers (SPIE) Conference Series*, Vol. 10707, Proc. SPIE, 107070K, doi: [10.1117/12.2314340](https://doi.org/10.1117/12.2314340)
- McLaughlin, D. B. 1924, *ApJ*, 60, 22, doi: [10.1086/142826](https://doi.org/10.1086/142826)
- Mékarnia, D., Guillot, T., Rivet, J. P., et al. 2016, *MNRAS*, 463, 45, doi: [10.1093/mnras/stw1934](https://doi.org/10.1093/mnras/stw1934)
- Nagasawa, M., Ida, S., & Bessho, T. 2008, *ApJ*, 678, 498, doi: [10.1086/529369](https://doi.org/10.1086/529369)
- Paredes, L. A., Henry, T. J., Quinn, S. N., et al. 2021, *AJ*, 162, 176, doi: [10.3847/1538-3881/ac082a](https://doi.org/10.3847/1538-3881/ac082a)
- Pepper, J., Kane, S. R., Rodriguez, J. E., et al. 2020, *AJ*, 159, 243, doi: [10.3847/1538-3881/ab84f2](https://doi.org/10.3847/1538-3881/ab84f2)
- Perryman, M. A. C., Lindegren, L., Kovalevsky, J., et al. 1997, *A&A*, 500, 501
- Petrovich, C. 2015, *ApJ*, 805, 75, doi: [10.1088/0004-637X/805/1/75](https://doi.org/10.1088/0004-637X/805/1/75)
- Petrovich, C., Tremaine, S., & Rafikov, R. 2014, *ApJ*, 786, 101, doi: [10.1088/0004-637X/786/2/101](https://doi.org/10.1088/0004-637X/786/2/101)
- Rasio, F. A., & Ford, E. B. 1996, *Science*, 274, 954, doi: [10.1126/science.274.5289.954](https://doi.org/10.1126/science.274.5289.954)
- Ricker, G. R., Winn, J. N., Vanderspek, R., et al. 2015, *Journal of Astronomical Telescopes, Instruments, and Systems*, 1, 014003, doi: [10.1117/1.JATIS.1.1.014003](https://doi.org/10.1117/1.JATIS.1.1.014003)
- Rossiter, R. A. 1924, *ApJ*, 60, 15, doi: [10.1086/142825](https://doi.org/10.1086/142825)
- Schmider, F.-X., Abe, L., Agabi, A., et al. 2022, in *Society of Photo-Optical Instrumentation Engineers (SPIE) Conference Series*, Vol. 12182, *Ground-based and Airborne Telescopes IX*, ed. H. K. Marshall, J. Spyromilio, & T. Usuda, 121822O, doi: [10.1117/12.2628952](https://doi.org/10.1117/12.2628952)
- Sedaghati, E., Jordán, A., Brahm, R., et al. 2023, *AJ*, 166, 130, doi: [10.3847/1538-3881/acea84](https://doi.org/10.3847/1538-3881/acea84)
- Sikora, J. T., Rowe, J. F., Splinter, J., et al. 2024, *arXiv e-prints*, arXiv:2407.12456, doi: [10.48550/arXiv.2407.12456](https://doi.org/10.48550/arXiv.2407.12456)
- Singh, V., Scandariato, G., Smith, A. M. S., et al. 2024, *A&A*, 683, A1, doi: [10.1051/0004-6361/202347533](https://doi.org/10.1051/0004-6361/202347533)
- Skrutskie, M. F., Cutri, R. M., Stiening, R., et al. 2006, *AJ*, 131, 1163, doi: [10.1086/498708](https://doi.org/10.1086/498708)
- Smith, J. C., Stumpe, M. C., Van Cleve, J. E., et al. 2012, *PASP*, 124, 1000, doi: [10.1086/667697](https://doi.org/10.1086/667697)
- Stumpe, M. C., Smith, J. C., Catanzarite, J. H., et al. 2014, *PASP*, 126, 100, doi: [10.1086/674989](https://doi.org/10.1086/674989)
- Stumpe, M. C., Smith, J. C., Van Cleve, J. E., et al. 2012, *PASP*, 124, 985, doi: [10.1086/667698](https://doi.org/10.1086/667698)
- Timpe, M., Barnes, R., Kopparapu, R., et al. 2013, *AJ*, 146, 63, doi: [10.1088/0004-6256/146/3/63](https://doi.org/10.1088/0004-6256/146/3/63)
- Tokovinin, A. 2018, *PASP*, 130, 035002, doi: [10.1088/1538-3873/aaa7d9](https://doi.org/10.1088/1538-3873/aaa7d9)
- Tokovinin, A., Fischer, D. A., Bonati, M., et al. 2013, *PASP*, 125, 1336, doi: [10.1086/674012](https://doi.org/10.1086/674012)
- Twicken, J. D., Catanzarite, J. H., Clarke, B. D., et al. 2018, *PASP*, 130, 064502, doi: [10.1088/1538-3873/aab694](https://doi.org/10.1088/1538-3873/aab694)
- von Zeipel, H. 1910, *Astronomische Nachrichten*, 183, 345, doi: [10.1002/asna.19091832202](https://doi.org/10.1002/asna.19091832202)
- Winn, J. N., Fabrycky, D., Albrecht, S., & Johnson, J. A. 2010, *ApJL*, 718, L145, doi: [10.1088/2041-8205/718/2/L145](https://doi.org/10.1088/2041-8205/718/2/L145)

Wu, D.-H., Rice, M., & Wang, S. 2023, AJ, 165, 171,
doi: [10.3847/1538-3881/acbf3f](https://doi.org/10.3847/1538-3881/acbf3f)
Zhang, J., Huber, D., Weiss, L. M., et al. 2024, arXiv e-prints,
arXiv:2407.21377, doi: [10.48550/arXiv.2407.21377](https://doi.org/10.48550/arXiv.2407.21377)

Zhou, G., Bakos, G. Á., Bayliss, D., et al. 2019, AJ, 157, 31,
doi: [10.3847/1538-3881/aaf1bb](https://doi.org/10.3847/1538-3881/aaf1bb)
Ziegler, C., Tokovinin, A., Briceño, C., et al. 2020, AJ, 159, 19,
doi: [10.3847/1538-3881/ab55e9](https://doi.org/10.3847/1538-3881/ab55e9)